

Article

Biobased Copolyamides 56/66: Synthesis, Characterization and Crystallization Kinetics

Chia-Hsiung Tseng and Ping-Szu Tsai *

Department of Chemical and Material Engineering, College of Engineering, National Kaohsiung University of Science and Technology, Kaohsiung 807618, Taiwan

* Correspondence: charles1@nkust.edu.tw

Abstract: This study synthesized a series of new biobased copolyamides (co-PAs), namely PA56/PA66 with various comonomer ratios, by using in situ polycondensation. The structures, compositions, behaviors, and crystallization kinetics of the co-PAs were investigated through proton nuclear magnetic resonance (^1H NMR) spectroscopy, gel permeation chromatography (GPC), Fourier transform infrared (FT-IR) spectroscopy, differential scanning calorimetry (DSC), polarized optical microscopy (POM), and X-ray diffraction (XRD). The influence of the composition of co-PAs on their mechanical properties and thermal stability was investigated. The co-PAs exhibited a eutectic melting point when the PA56 content was 50 mol%, with the crystallization temperature decreasing from 229 to a minimum 188 °C and the melting temperature from 253 to a minimum 218 °C. The results indicated that the tensile strength and flexural modulus first decreased and then increased as the PA66 content increased. The nonisothermal crystallization kinetics of the PA56/PA66 co-PAs were analyzed using both the Avrami equation modifications presented by Jeziorny and Mo. The results also indicated that the crystallization rate of the PA56/PA66 co-PAs was higher than that of PA56.

Keywords: biobased copolyamide; differential scanning calorimetry; eutectic behavior; nonisothermal crystallization kinetics



Citation: Tseng, C.-H.; Tsai, P.-S. Biobased Copolyamides 56/66: Synthesis, Characterization and Crystallization Kinetics. *Polymers* **2022**, *14*, 3879. <https://doi.org/10.3390/polym14183879>

Academic Editors: Palraj Ranganathan and Bhuvanenthiran Mutharani

Received: 17 August 2022

Accepted: 13 September 2022

Published: 17 September 2022

Publisher's Note: MDPI stays neutral with regard to jurisdictional claims in published maps and institutional affiliations.



Copyright: © 2022 by the authors. Licensee MDPI, Basel, Switzerland. This article is an open access article distributed under the terms and conditions of the Creative Commons Attribution (CC BY) license (<https://creativecommons.org/licenses/by/4.0/>).

1. Introduction

Polymers derived from petroleum, natural gas, and coal have been extensively used but these conventional fossil resources are non-renewable and limited. In addition, negative externalities such as air, water, and land pollution and global warming necessitate the transition of all fossil-fuel dependent sectors to sustainable and renewable alternatives. Therefore, biobased polymers are gradually attracting considerable attention as a leading scientific and technological innovation for global economic development owing to their green, environmentally friendly, and resource-saving features that contribute to sustainable development. Polyamides (PAs) are excellent engineering thermoplastic engineering materials, which are extensively used in industrial applications. Semicrystalline PA66 is another commercialized PA that was developed by Carothers in 1936 [1] and has been extensively used in several engineering applications, including the production of membranes, films, textile fibers, electronics (e.g., connectors, surface mount devices, and reflectors), flexible packaging materials for food, and plastics for use in the automotive industry [2–6]. These applications are possible because of the excellent mechanical strength, dimensional stability at high temperature, chemical resistance, and other advantages afforded by PA66. PAs are becoming increasingly crucial as high-performance polymers. Several all-biobased PAs such as PA11, PA1010, and PA410, or partly biobased PAs such as PA610 and PA1012 with excellent engineering applicability, have been commercialized [7]. The biobased PAs such as PA52, PA54, PA56, PA510, and 5T (denoted as PA5X) are synthesized from 1,5-diaminopentane and diprotic acid through a green process [8–13]. 1,5-Diaminopentane is used to derive bio-PAs from renewable feedstocks to replace conventional PAs derived

from petrochemical routes. Gale and Epps discovered that lysine decarboxylase from *Escherichia coli* can be used in acid stress-induced processes [14], thereby facilitating biobased cadaverine production. Microbial production of cadaverine has been observed in recombinant *E. coli* and *Corynebacterium glutamicum* strains, as indicated by plasmid- or genome-based heterologous expression of *E. coli cadA* and *ldcC* that encode inducible and constitutive lysine decarboxylase, respectively [15–17]. Although PA56 is biobased, it can be synthesized through the polycondensation reaction of adipic acid (AA) and 1,5-pentamethylenediamine (PMD). PA56 has been tested in the downstream sectors of the petroleum industry, not only as a renewable alternative to traditional materials, but also as a novel and unique polymer for membranes, industrial plastics, and textile markets. PA56 is characterized by high chemical resistance, melting temperature, modulus, intrinsic flame resistance, ultraviolet light stability, dyeability, and moisture absorption and can be used in applications such as industrial yarns and filaments [18–21]. However, the modification of its molecular structure has received little attention. In this work, we used PA66 to modify PA56 by in situ polymerization. The crystallization of PA56 in copolymers is usually affected not only by processing conditions but also by PA66. There is a need to design new PA56-based copolymers to reduce production costs while also maintaining or improving their mechanical, molding, thermal, and heat resistance properties.

Copolymerization methods have been extensively applied in polymer modification owing to their simplicity and efficiency. Target polymers with desirable properties can be synthesized by selecting appropriate comonomers and molecular designs [22–25]. Moreover, the use of biobased raw materials as comonomers promotes sustainable development. Considerable effort has been dedicated to preparing co-PAs from biobased comonomers [26–28]. Co-PAs crystallinity depends on the degree of symmetry, lengths between amide groups and orientation of amide groups (odd–even effect). In a characteristic plot of the copolymer melting temperature and enthalpy versus composition, if the melting temperatures of a copolymer do not lie at the local minimum as a function of composition, then the corresponding comonomers can be considered to be isomorphous, (e.g., the co-PA of AA and terephthalic acid in PA46/6T). PA46/6T exhibits similar lengths between the amide groups of AA and units of terephthalic acid, enabling its incorporation into the same crystal structure without inducing changes in the crystal lattice dimensions [29,30]. A local minimum indicates that the comonomer is an impurity that decreases the melting point, size, and perfection of the formed crystals and the comonomers are not co-crystalline and thus do not fit into the same crystalline lattice. Novitsky reported that neither PA10T nor PA12T is co-crystalline with PA6T. The lengths of PA10T and PA12T between the amide units are different from PA6T, and this limits the incorporation of the PA6T. A decrease in melting temperature up to 30 wt% PA6T promotes the formation of fewer and smaller or less perfect crystals [31]. However, when two crystalline polymers are copolymerized, isodimorphism occurs and is characterized by changes in crystal lattice dimensions at the eutectic point. The comonomer PA6T can be incorporated into a crystal structure that is different from its own. The degree of melting point depression and amount of crystallinity at the eutectic point are functions of the structural similarity of the repeating units of the comonomer [32,33].

In this study, a series of PA56/PA66 co-PAs with different PA56/PA66 ratio compositions were synthesized through in situ polymerization. The structure and properties of the PA56/PA66 co-PAs were comprehensively investigated using wide-angle X-ray diffraction (XRD), gel permeation chromatograph (GPC), Fourier transform infrared (FT-IR) spectroscopy, and proton nuclear magnetic resonance ($^1\text{H-NMR}$) spectroscopy. Moreover, the thermal and mechanical properties of the co-PAs were systematically investigated using differential scanning calorimetry (DSC), polarized optical microscopy (POM), thermogravimetry analysis (TGA), and tensile and flexural tests. The co-PAs were subjected to practical processes, namely, molding, extrusion and film or fiber formation, under non-isothermal and dynamic conditions. Furthermore, the nonisothermal crystallization of

the co-PAs was quantitatively examined in an industrial environment to optimize their processing conditions and improve their properties.

DSC is an excellent tool to measure the kinetics of nonisothermal crystalline polymerization. However, nonisothermal studies are complex and therefore require more care. In order to solve the above issues and obtain appropriate kinetic data, the Kinetics Committee of the International Confederation for Thermal Analysis and Calorimetry (ICTAC) has provided some advice and guidance [34,35]. The recommendations offer guidance for obtaining kinetic data that are adequate to the actual kinetics of various processes, including crystallization of polymers, and focus on kinetic measurements performed by means of thermal analysis methods such as thermogravimetry (TG) or thermogravimetric analysis (TGA), differential scanning calorimetry (DSC), and differential thermal analysis (DTA).

The Avrami equations modified by Jeziorny and Mo were employed to evaluate the nonisothermal crystallization kinetics of the PA56/PA66 co-PAs.

2. Experimental Section

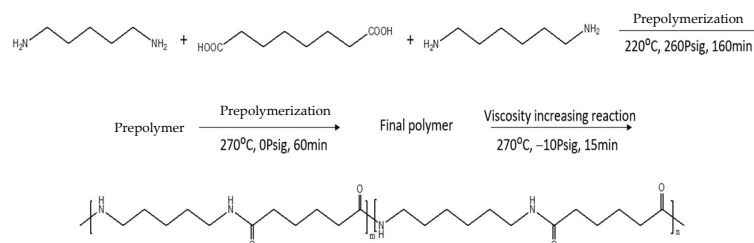
2.1. Materials

Biobased PMD (>99.7%) was procured from Cathay Biotech Inc. (Shanghai, China). 1,6 Hexamethylenediamine (HMD; >99.7%) was procured from INVISTA (Vitoria, TX, USA). AA (>99.8%) was procured from Huafeng Group Co., Ltd., (Chongqing, China) and sodium hypophosphate (SHP) was obtained from Fuerxin Pharmaceutical and Chemical (Shangrao, Jiangxi, China).

2.2. Method

2.2.1. Synthesis of PA56/PA66 Co-PA Salt

The co-PA salts of PA56 and PA66 were prepared through salt reactions of PMD and HMD with individual AA samples, as illustrated in Scheme 1. Six compositions of PA56/PA66 were prepared (100/0, 70/30, 50/50, 30/70, 10/90 and 0/100), and by molar ratios are presented in Table 1, with the 100/0 composition representing PA56 and the 0/100 composition representing PA66. The intermediate compositions presented random copolymers between PA56 and PA66. A 1-wt% diluted SHP aqueous solution was used as the catalyst. Weighted quantities of PMD, AA, and distilled water were added to a 10 L autoclave equipped with a stirrer, a gas inlet and an outlet. The mixture in the autoclave was stirred for 1 h at 30 °C to obtain the PA56 salt. The PA66 salt was prepared in a similar manner. After the completion of the salt preparation processes, weighted quantities (Table 1) of PA56, PA66, and SHP were added to an autoclave filled with nitrogen and agitated at 50 rpm. The co-PA salts were thus synthesized in accordance with the aforementioned approximately 1 h.



Scheme 1. The synthetic route of PA56/66 copolyamide.

Table 1. Sample code and composition of PA56/66 copolyamides.

Sample Code	Nylon 56/66 (mole%)	PMD (mole)	HMD (mole)	AA (mole)	SHP (ppm)
PA56	100/0	1	0	1	80
CoPA-1	70/30	0.7	0.3	1	80
CoPA-2	50/50	0.5	0.5	1	80
CoPA-3	30/70	0.3	0.7	1	80
CoPA-4	10/90	0.9	0.1	1	80
PA66	0/100	0	1	1	80

2.2.2. Synthesis of PA56/PA66 Co-PAs

The melt condensation polymerization process involved three stages: boiling of water, polymerization, and reactions for increasing viscosity. First, the autoclave was heated to 220 °C in 0.5 h and maintained at the temperature for approximately 100 min. During the heating process, the highest pressure of the autoclave was maintained at 260 psig by discharging steam. Subsequently, the pressure of the autoclave was gradually decreased to atmospheric pressure level, and the temperature was increased to 270 °C in 1 h. After the reaction, the pressure of the polymerization autoclave was decreased to −10 psig in 15 min, thereby increasing the viscosity. After the completion of the polycondensation process, the co-PAs were cooled, shaped into pellets using a pelletizing water cutter, and washed with distilled water. The co-PAs were added to a beaker and dried overnight in a vacuum oven at 80 °C. The prepared PA56/PA66 co-PAs were composed of 100, 70, 50, 30, 10, and 0 mol% PA56 and are denoted herein as PA56, CoPA-1, CoPA-2, CoPA-3, CoPA-4 and PA66, respectively.

2.3. Characterization

2.3.1. DSC Measurements

DSC was executed using a Perkin–Elmer DSC-7 instrument (Waltham, MA, USA) to analyze the melting behavior and crystallization kinetics of the co-PAs. All DSC measurements were performed under nitrogen at a flow rate of 20 mL·min^{−1} and calibrated relative to a high-purity indium standard; samples weighing 3 and 5 mg were used to minimize the effect of low PA thermal conductivity. To determine the melting temperatures and crystallization temperatures, the co-PA samples were heated to 300 °C at a constant rate 20 °C·min^{−1} for 5 min to eliminate residual crystals; the samples were then rapidly cooled to 15 °C (at −10 °C·min^{−1}) to obtain the cooling curve. In the final stage, the samples were heated to 300 °C (at 10 °C·min^{−1}) to obtain the heating curve.

2.3.2. FT-IR and ¹H-NMR

The room-temperature ¹H NMR spectra of the PA56/PA66 copolymers were obtained using a JEOL ECZ600R 600 MHz spectrometer (Tokyo, Japan). The FTIR spectra were recorded using a PerkinElmer FTIR instrument (Waltham, MA, USA). At least 32 scans were performed for each sample to obtain spectra at a spectral resolution of 2 cm^{−1} within the wavelength range of 600–4000 cm^{−1} by using a KBr disc.

2.3.3. Gel Permeation Chromatography (GPC)

The number average molecular weight (M_n), weight average molecular weight (M_w), and polydispersity index (PDI) of the PA56/66 copolyamides were determined via the gel permeation chromatography (GPC) device from a Waters alliance system (Malvern Ltd., Malvern, UK) with refractive index (RI) and water high-resolution (HR) column at a flow rate of 0.6 mL/min and injection column of 250 µL. Column temperature was held at 35 °C. The well-characterized narrow poly(methyl methacrylate) (PMMA) in hexafluoroisopropanol (HFIP) was used as the calibration.

2.3.4. TGA Measurements

TGA was performed using a TGA550 thermobalance (TA Instruments, New Castle, DE, USA). Samples weighing 9–11 mg were placed in a platinum pan in a nitrogen atmosphere and heated from 25 to 800 °C at a rate of 10 °C·min⁻¹. The characteristic degradation temperature of the derivative thermogravimetric curve was determined at a 5% weight loss ($T_{d-5\%}$).

2.3.5. Polarized Optical Microscopy (POM)

The spherulitic morphology of the PA56/PA66 co-PAs was observed using a Nikon LV100ND (Tokyo, Japan) polarized optical microscope equipped with a LINKAM LTS420 (Surry, UK) hot stage and a DS-Fi3 camera system. The samples were sandwiched between two microscopic slides and melted at 300 °C for 5 min and then cooled to 200 °C at -10 °C·min⁻¹; the images of the samples were captured at different times and after crystallization. This process was accompanied by the appearance and growth of spherulites.

2.3.6. X-ray Diffraction (XRD)

The XRD patterns of the PA56/PA66 co-PAs were obtained using an X-ray diffractometer system (Rigaku, D/MAX, Tokyo, Japan) equipped with linear monochromatic Cu-K α radiation ($\lambda = 0.154$ nm) at ambient temperature and operated at 40 kV and 200 mA. The system was operated within a 2θ range of 5–50° and at a scanning speed of 5° min⁻¹.

2.3.7. Mechanical Properties

Tensile strength and flexural strength tests were performed using a universal testing machine (Z010, Zwick, Ulm, Germany). The sample used for the measurements was 3.25 mm thick, 10 mm wide, and 114 mm long. The crosshead speed was set to 20 mm/min.

2.3.8. Nonisothermal Crystallization Process

The nonisothermal crystallization kinetics of the PA56/PA66 co-PAs were investigated. The samples were rapidly heated from 15 to 300 °C at 80 °C·min⁻¹ and then melted for 10 min at 300 °C to erase their thermal history. Subsequently, the samples were cooled to 15 °C at the five different cooling rates: 2.5, 5, 10, 20 and 40 °C·min⁻¹. The exothermal curves of heat flow as a function of temperature were recorded.

3. Results and Discussion

3.1. Characterization of PA56/66

FT-IR spectroscopy was conducted to obtain detailed information about the structures of PA56/PA66 co-PAs on the basis of the characteristic vibration energies of various molecular groups. Figure 1 displays the FT-IR spectrum of PA56, PA66, and a series of PA56/PA66 co-PAs, revealing characteristic bands ascribed to aliphatic PAs. The bands at approximately 3295 and 3086 cm⁻¹ were attributed to the N-H stretching vibrations in the crystalline and amorphous parts. The bands at approximately 2930 and 2858 cm⁻¹ were attributed to N-H in-plane bending vibrations (symmetric and asymmetric). The peaks at approximately 1630 cm⁻¹ were attributed to C=O stretching vibrations (amide I). Moreover, bands corresponding to N-H bending and C-N stretching vibrations (amide II) were observed by 1536 cm⁻¹ and resembled those corresponding to the α form bonds of various nylon structure, reported by Arimoto, Bradbury and Elliott [36]. Bands were also observed at 1464 and 1417 cm⁻¹ and were ascribed to deformation vibrations of CH₂ adjacent to N-H and C=O groups, respectively. A band was also noted at 936 cm⁻¹ and resembled a typical band for PA56 and PA66 macromolecules; this band was ascribed to C-C(O) stretching vibration. All FT-IR spectra indicated that the synthesized PA56/PA66 co-PAs possessed desirable properties. The differences between the spectra obtained for the PA56, PA66 and PA56/PA66 co-PAs were negligible [37–41].

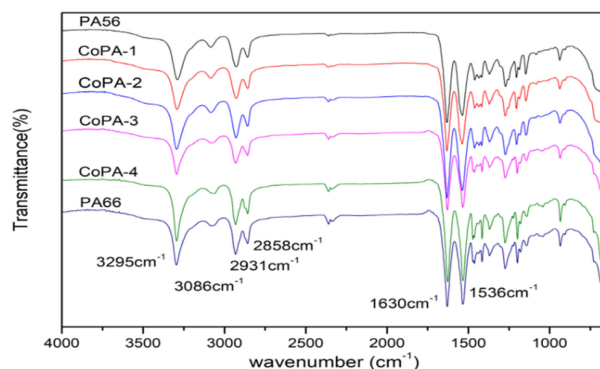


Figure 1. FTIR spectra of the PA56/66 copolyamides.

The chemical structures of the PA56/PA66 copolymers were analyzed using $^1\text{H-NMR}$ spectroscopy, as displayed in Figure 2. Signals were observed at approximately 3.3 ppm (a) and 2.4 ppm (b) and were ascribed to the methylene of the adipate unit. Moreover, signals were observed at approximately 1.9 ppm ($e + h$), 2.3 ppm ($d + g$), and 4.0 ppm ($c + f$) and corresponded to the methylene in hexanediamine and pentanediamine units. Overlapping characteristic peaks were observed, and these were attributed to the high similarity between hexanediamine adipate and pentanediamine adipate. However, the enhancement of the signal strengths of peaks ($e + h$) for all samples corresponded to an increase in hexanediamine adipate content, similar to the increase in the feed ratio of hexanediamine during polycondensation reactions [42–44]. The integral areas of resonance peak could be used to confirm the composition of PA56/66 copolyamides from the signal integrals of peaks at a , b , ($d + g$), and ($e + h$) using the following equations, for which the results are presented in Table 2 [44].

$$b + (d + g) - a = 4x + 4y \quad (1)$$

$$e + h = 4x + 2y \quad (2)$$

$$\text{PA56} = \frac{y}{x + y} \times 100\% ; \text{PA66} = \frac{x}{x + y} \times 100\% \quad (3)$$

where, x and y are the mole% of PA56 and PA66, respectively. The ratios of integral areas of the proton peaks in $^1\text{H-NMR}$ spectra were approximately equal to the composition, which proved that the chemical structures of the PA56/PA66 co-PA match the expectation.

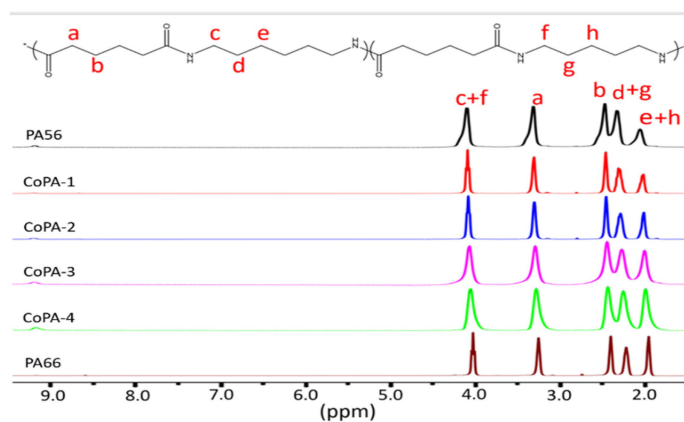


Figure 2. ^1H NMR spectra of PA56, PA66 and PA56/66 copolyamides.

Molecular weight and its distribution of the synthesized PA/56/66 co-PAs were characterized by GPC. The calculated number average molecular weight, weight average molecular weight, was shown in Table 2. It can be seen clearly that molecular weight between acceptable values for polycondensation polymers; specifically, values were be-

tween 19,700–33,400 g/mol and 43,600–53,600 g/mole for M_n and M_w , respectively. A well relationship was found: the lower values were detected for PA56/PA66 co-PAs with an intermedia composition and higher values for neat PA56 and PA66. The M_n and M_w of CoPA-2 were much lower, and molecular weight distribution also known as polydispersion index (PDI) was 2.21, higher than other co-PAs. The larger the PDI, the broader the molecular weight. The main reason for this phenomenon is the co-PA becomes more irregular and the CoPA-2 is more disordering.

Table 2. $^1\text{H-NMR}$ and Molecular weights of PA56/66 copolyamides.

Sample	Feed Ratio ^a	Calculated ^b	M_n , g/mol	M_w , g/mol	PDI
PA56	100	-	31,500	52,300	1.66
CoPA-1	70/30	72.53/27.46	24,600	43,800	1.78
CoPA-2	50/50	51.35/48.64	19,700	43,600	2.21
CoPA-3	30/70	25.44/74.56	25,700	47,600	1.85
CoPA-4	10/90	11.53/88.46	32,200	52,300	1.63
PA66	100	-	33,400	53,600	1.61

^a PMD/HMD; ^b PA56 segment/PA66 segment by $^1\text{H-NMR}$.

3.2. Thermal Properties of PA56/PA66

Figure 3a displays the TGA curves derived for the PA56/PA66 co-PAs as well as the temperatures corresponding to a weight loss of 5 wt% ($T_{d-5\%}$), which ranged between 298.0 and 383.5 °C. The neat PA56, PA66 and their copolyamides have slight weight loss at 100 °C, which are 0.769%, 0.661%, 0.619%, 0.813%, 0.339% and 0.555 wt%, respectively. This phenomenon due to the evaporation of free water in copolyamides, and after the temperature 100 °C, there is still continuous weight loss, which is caused by the evaporation of crystal water in the polyamide. This crystal water is the formation of hydrogen bonds between the water molecules and the amide end of the polyamide. As indicated in this figure, the obtained co-PAs possessed excellent thermal stability because the $T_{d-5\%}$ values of all PA56/PA66 co-PAs were over 300 °C except for that of CoPA-2, which was 298 °C. All curves exhibited one stage of weight loss. The $T_{d-5\%}$ value of CoPA-2 was lower than those of the other samples; the $T_{d-5\%}$ value first decreased and then increased as the mole percent of PA66 increased (Table 3). The CoPA-2 sample did not form perfect crystals at the eutectic point of the PA56/PA66 co-PAs. The values of the extrapolated onset temperature (T_{onset}), temperature at the maximum rate of decomposition (T_{max}), temperature at 50% weight loss ($T_{50\%}$), and residue at 600 °C are listed in Table 3. T_{max} was obtained according to the DTG curves, as displayed in Figure 3b. The T_{max} values of the samples ranged from 442.8 to 457.0 °C, and CoPA-2 had the lowest T_{max} value. The amounts of residue of PA56 and PA66 were higher than those of all PA56/PA66 co-PAs, indicating that the homo-PAs possessed strong H bonding and more perfect crystalline structures [45,46].

Table 3. TGA and DTG results for the PA56/66 copolyamides.

Sample	$T_{d-5\%}$ (°C)	T_{onset} (°C)	$T_{50\%}$ (°C)	T_{max} (°C)	Residue at 600 °C (%)
PA56	348	413	440	445	3.02
CoPA-1	333	415	441	452	1.98
CoPA-2	298	415	442	443	1.77
CoPA-3	319	416	443	479	2.83
CoPA-4	383	417	444	444	1.93
PA66	379	423	450	457	4.64

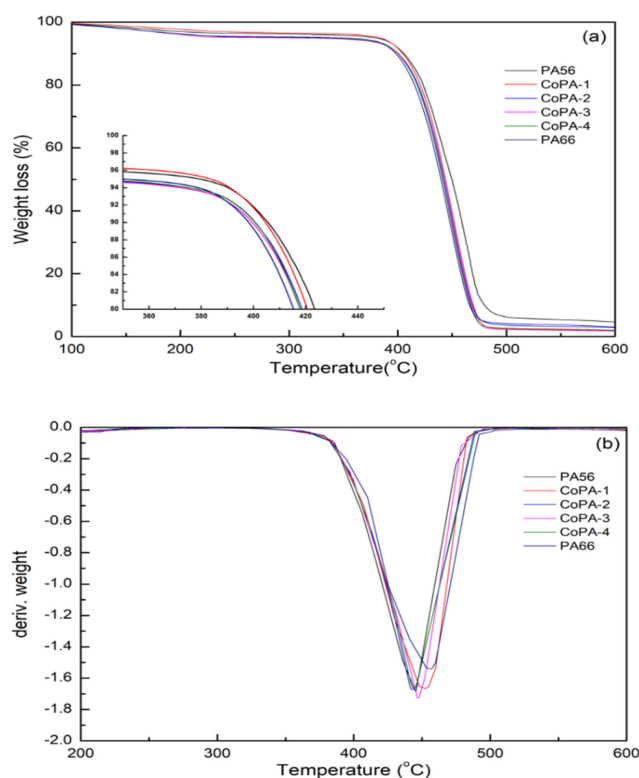


Figure 3. TGA (a) and DTG (b) curves of PA56/PA66 copolyamides with different comonomer ratios.

3.3. Differential Scanning Calorimetry (DSC)

The second heating DSC curves of PA56, PA66 and PA56/66 co-PAs after cooling at DSC $10\text{ }^{\circ}\text{C}\cdot\text{min}^{-1}$ from the molten states are shown in Figure 4. The results of DSC are listed in Table 4. The results show that the melting behavior of PA56 is more complicated by comparison with that of PA66. As illustrated in Figure 4a, the melting curves of the CoPA-1, CoPA-2, and CoPA-3 samples exhibited double-melting endotherms, which are common for PAs, and a recrystallization phenomenon was observed [47]. The melting temperatures of PA56 and PA66 were 253 and 261 $^{\circ}\text{C}$, respectively, and the crystallization temperatures were 208 and 229 $^{\circ}\text{C}$, respectively. In the range of PA56 content of 0–50 mol%, the melting temperature and crystallization temperature of co-PAs showed an approximate linear decrease trend with the increase in PA66 content, and the lowest T_m and T_c values were observed for CoPA-2, which were 218 and 188 $^{\circ}\text{C}$, respectively, as shown in Figure 4c. Similarly, the observed melting enthalpies (H_m), crystallization enthalpy (H_c) and glass transition temperature (T_g) of co-PAs with an intermedia composition were lower compared to that of neat PA56 and PA66, the (H_m (50.6 $\text{J}\cdot\text{g}^{-1}$), (H_c ($-46.9\text{ J}\cdot\text{g}^{-1}$) and T_g (54.2 $^{\circ}\text{C}$) values of the CoPA-2 are lowest. The above phenomenon describes how when more PA66 units are introduced into the PA56 molecular chain, the ordered arrangement of the PA56 molecular chain is destroyed, and the co-PA structure becomes more irregular; this results in crystal defects and the formation of small crystals, reducing the crystallization ability and adversely affecting the melting temperature. At 50 mol% PA66, PA56/PA66 forms a eutectic point, and the copolymer chain structure is the most disordered. The main reason for this is that there is a significant chain length difference between PMD and HMD, and after HMD replaces PMD, the asymmetric hydrogen bonds and the conformation of the chain are broken [31,48]. When PA66 exceeds 50 mol%, the T_m and T_c values of co-PAs also increase with the increase in PA66 content, and the melting and crystallization behaviors of co-PAs gradually tend to the pure PA66.

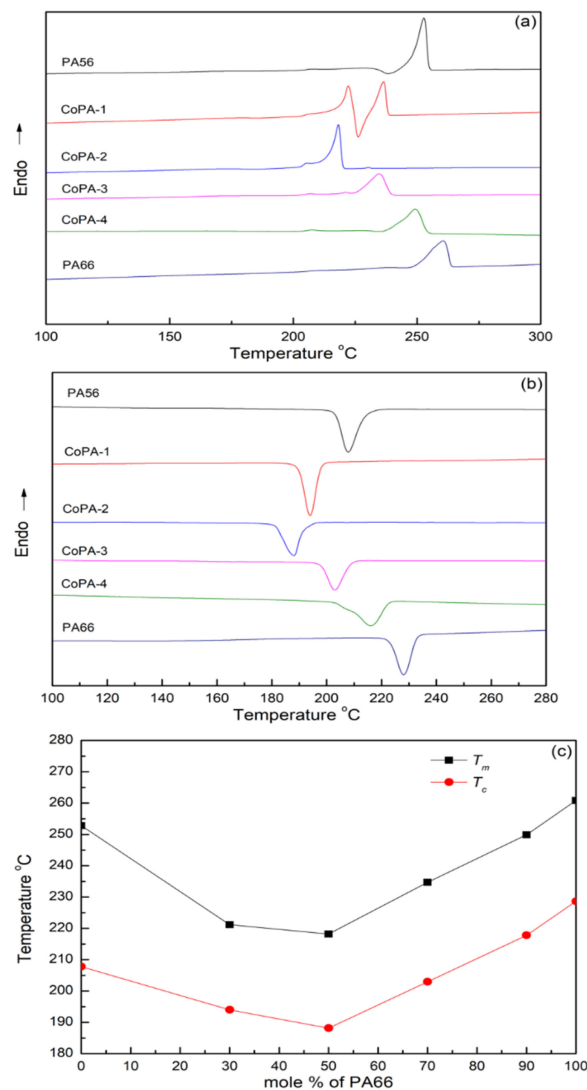


Figure 4. DSC thermographs of PA56/66 copolyamides; (a) heating curves (b) cooling curves (c) melting temperatures and crystallization temperatures.

Table 4. The thermal properties of PA56/PA66 copolyamides by DSC.

Sample	T_g (°C) ^a	T_{m1} (°C) ^b	ΔH_{m1} (J·g ⁻¹) ^b	T_{m2} (°C) ^b	ΔH_{m2} (J·g ⁻¹) ^b	T_c (°C) ^c	ΔH_c (J·g ⁻¹) ^c
PA56	60.3	252.8	57.6	-	-	207.8	-55.5
CoPA-1	56.4	222.2	90.9	236.5	53.8	194	-53.5
CoPA-2	54.2	218.2	50.6	205.2	1.3	188.1	-46.9
CoPA-3	56.8	234.7	52.1	206.7	1.0	203.0	-48.2
CoPA-4	59.3	249.9	55.7	207.5	1.1	217.8	-51.0
PA66	64.0	260.9	60.6	-	-	228.7	-63.0

^a T_g : Glass transition temperature by DSC; ^b T_{m1} , T_{m2} , (H_{m1} , H_{m2}): the first and second melting temperature and the melt enthalpy were determined in the second heating scan, respectively; ^c T_c , (H_c): the crystallization temperature and crystallization enthalpy determined in the cooling scan.

3.4. Crystal Structure of PA56/PA66

Bunn and Garner reported that nylon 66 and nylon 610 possess triclinic structures consisting of fully extended chains connected by hydrogen bonds and that their X-ray diffractograms exhibit two characteristic peaks at room temperature [49]. Most even–even nylon materials possess α -form crystals at room temperature. The main characteristic

diffraction peak of γ -crystalline PAs is a near-hexagonal unit cell with a diffraction peak at approximately $2\theta = 21.0^\circ$. Crystalline forms have been observed for odd–odd, odd–even and even–odd PAs [50]. In this study, XRD (Figure 5) was used to analyze the crystallization of the PA56/PA66 co-PAs. As displayed in Figure 5, the XRD pattern of PA56 and CoPA-1 exhibited strong reflections at $2\theta = 21.22^\circ$ and 23.39° , respectively and weak reflections at $2\theta = 21.13^\circ$ and 24.17° , respectively; the strong reflections at $2\theta = 21.22^\circ$ and 23.39° corresponded to the (020) and (010) crystallographic planes, respectively and the weak reflections at $2\theta = 21.13^\circ$ and 24.17° corresponded to typical γ and α crystal forms, respectively. However, only one strong diffraction peak was observed for CoPA-2 at $2\theta = 21.61^\circ$, similar to the diffraction peaks observed for the γ -crystalline phase of PA56 reported by Puiggali and colleagues [51,52]. With an increase in PA66 units, the characteristic diffraction peaks observed for PA56/PA66 broadened, and their intensity decreased. This is because low levels of PA56 disrupted PA66 crystal formation. Beyond the eutectic point at 50 mol% PA66, the two diffraction peaks reappeared, and the WAXD patterns gradually became similar to that of PA66 with a further increase in PA66 content. The XRD spectra of CoPA-3 and CoPA-4 are displayed in Figure 5; maximum peaks were observed at $2\theta = 20.38^\circ$, 23.36° and 20.74° , 23.09° , respectively, which corresponded to the (100) and (010)/(100) crystallographic planes, similar to those observed for PA66 ($2\theta = 20.74^\circ$ and 23.42°), indicating the presence of the α -crystalline phase (Figure 5). The PA56 and PA66 segments complemented each other during the crystallization process. The WAXD patterns exhibited a characteristic peak for PA56 when the PA56 content was dominant. The regular arrangement of the amide bonds in the PA66 segments was broken, hindering the crystallization of the PA56 molecular chain. For PA66, a characteristic crystallization peak began to appear when the PA66 content was adequate to form a longer fragment.

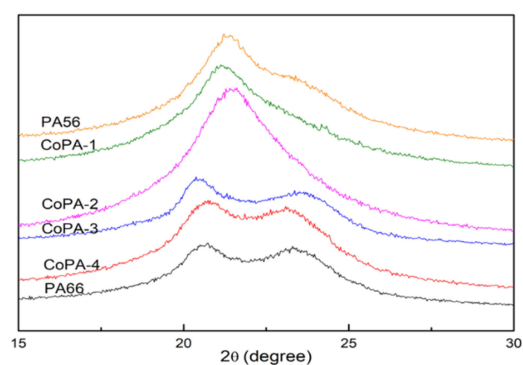


Figure 5. WAXS scans for PA56/66 copolyamides.

3.5. Mechanical Properties

Figure 6 illustrates the effects of PA56 on the mechanical properties of the samples. The tensile strength and flexural strengths at different PA56/PA66 ratios were determined to be within the ranges 71.6–86.7 and 117.0–136.4 MPa, respectively. The tensile/flexural strengths of neat PA56 and PA66 were 80.4/131.7 MPa and 86.7/136.4 MPa, respectively, and those of the copolymers exhibited an approximately linear decreasing trend to where the PA66 content was 0–50 mol%. When the PA66 content exceeded 50 mol%, the tensile strength and flexural strength of the co-PAs gradually increased and tended toward those of neat PA66. The molecular structure and crystal form of copolyamide directly determine the mechanical properties of the copolyamide. Compared with hexamethylenediamine, the comonomer pentamethylenediamine has one less methylene group in the molecule, and PA56 is an odd–even polyamide, and its asymmetric structure will influence the structural properties of PA56/66 co-PAs. The addition of the PA66 segment to PA56 increased the disordering of PA56, resulting in a decrease in the mechanical properties of co-PAs. When the PA56 content reaches 50%, the CoPA-2 copolyamide has the most disordered sequence structure, the lowest tensile strength and flexural strength (Figure 6). As shown in Table 4, the melting temperature T_m and glass transition temperature T_g of the coPA-2 is lower than

other co-PAs. The PDI of Co-PA2 is higher, and a wider molecular weight distribution leads to the poor mechanical property.

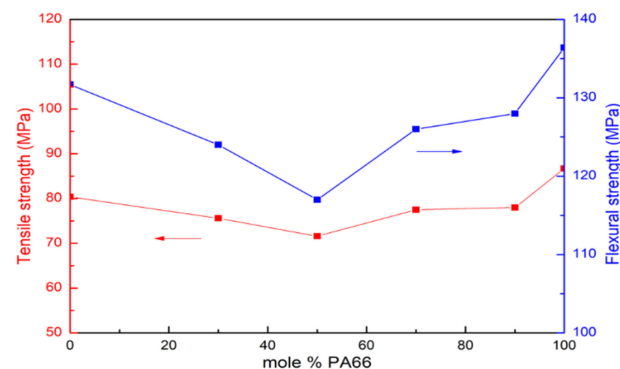


Figure 6. The tensile strength and flexural strength of PA56/66 copolyamides.

In addition, it can be seen from Figure 7c that the structure of CoPA-2 also presents more and smaller spherulites, resulting in more grain boundaries and surface area, so CoPA-2 is easily destroyed by external force. When the PA66 content exceeded 50 mol%, as the content of the PA66 segment increased continuously, the disordering decreased, the melting temperature T_m and glass transition temperature T_g increases again, the tensile strength and flexural modulus tended toward those of neat PA66.

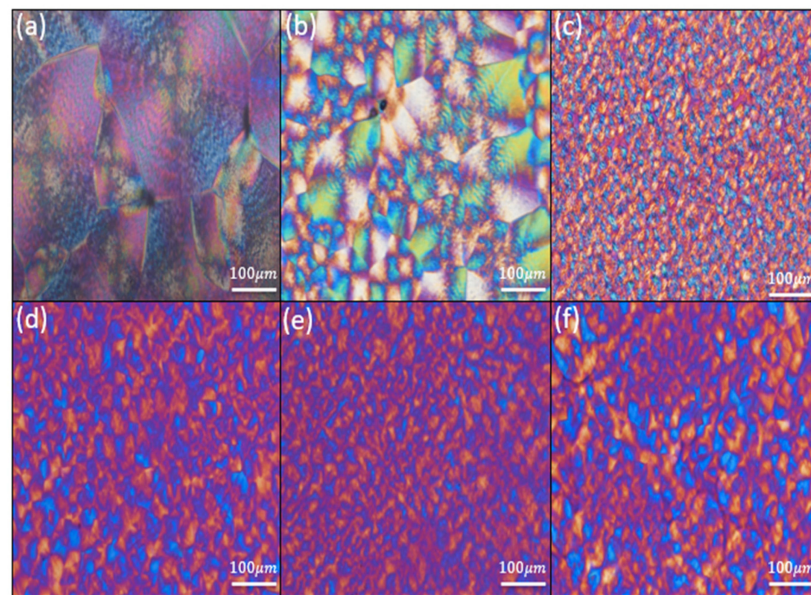


Figure 7. Polarized optical micrographs for PA56/66 copolyamides annealed at 300 °C for 5 min and slow-cooled off of (a) PA56, (b) CoPA-1, (c) CoPA-2, (d) CoPA-3, (e) CoPA-4 and (f) PA66.

3.6. Crystallite Morphology

POM is among the most predominant and effective tools for investigating spherulitic morphologies [53–56]. Figure 7 compares the polarized optical micrographs of the neat PA56, neat PA66 and co-PAs after they had been melted at 300 °C, annealed for 5 min, and then quenched to $T_c = 200$ °C at 10 °C·min⁻¹. From this figure it can be clearly seen there is a large variation in the size and morphology of spherulites in all the samples. For the neat polymer PA56, well-defined large, impinged Maltese cross spherulites were observed, as illustrated in Figure 7a. However, a dense granular texture of crystals was formed for the PA56/PA66 co-PAs, and the sizes of the crystalline grains were smaller. These results thus demonstrate that the number of crystal nuclei increased and the growth rate of

crystalline grains increased with the PA66 content. The spherulites in the CoPA-2 sample, as displayed in Figure 7c, were more uniform than those in the other co-PA. The CoPA-2 sample exhibited the smallest structure. PA56, PA66, and the co-PAs were supercooled at a specific temperature to allow crystal growth in order to observe and compare their morphologies clearly during the crystallization process, as shown in Figure 8. The crystal size of CoPA-1 was smaller than that of neat PA56, indicating that a large proportion of the nucleus was generated in a short period and that the growth of the crystal was restrained.

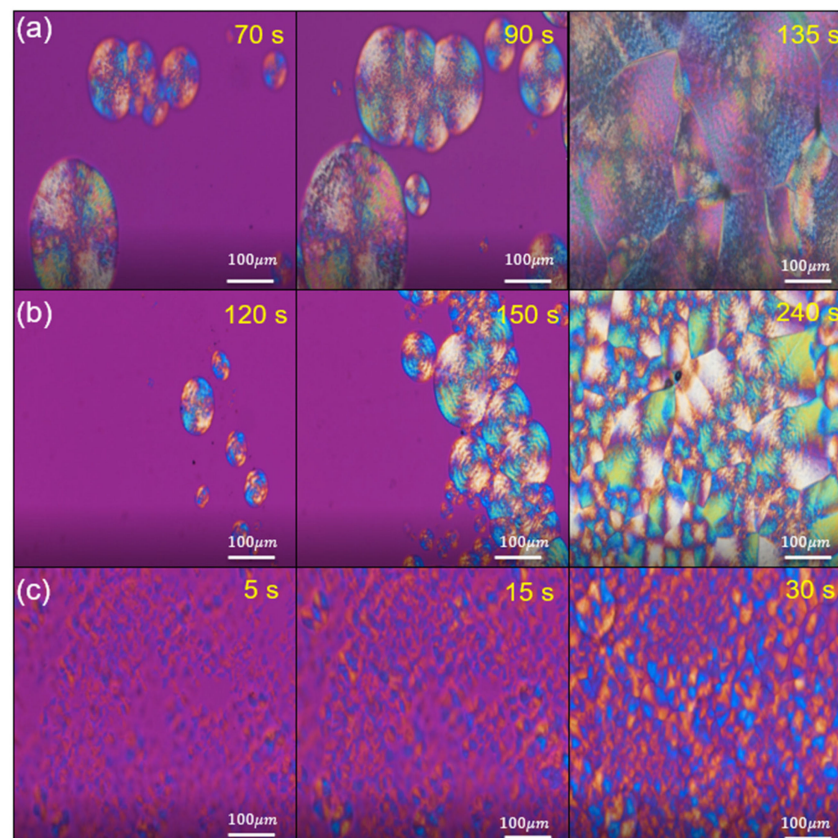


Figure 8. Optical micrographs of crystallized at different times of (a) PA56, (b) CoPA-1 and (c) PA66.

3.7. Nonisothermal Crystallization Kinetics

To study the nonisothermal crystallization kinetics of PA56/PA66 co-PAs, the relative crystallinity $X(t)$ was determined using the following equation:

$$X(t) = \frac{Q_t}{Q_\infty} = \frac{\int_{T_0}^T \left(\frac{dH_c}{dt} \right) dt}{\int_{T_0}^{T_\infty} \left(\frac{dH_c}{dt} \right) dt} \quad (4)$$

where the T_0 and T_∞ are crystallization onset and end temperature, respectively. T is an arbitrary temperature and dH_c/dt is the heat flow rate; Q_t is the heat generated at temperature T ; Q_∞ is the total heat generated during the final crystallization process. Figure 9 displays the nonisothermal crystallization exothermic peaks observed for a series of the PA56/PA66 co-PAs obtained under different cooling rates Φ ; the crystallization peak temperature T^* values, crystallization peak times t_{max} and relative crystallinity levels are summarized in Table 5. It could be found that T^* shifted to a lower temperature region and became wider as the cooling rate increased from Figure 9. The relative crystallinity $X(t)$ values obtained at different cooling rates through DSC are illustrated in Figure 10. A series of reversed S-shaped curves was observed, and these were attributed to spherulite impingement in the final crystallization stage; moreover, the curves tended to flatten.

The crystallization time and crystallization temperature can be formulated as follows (Figure 10):

$$t = \frac{|T_0 - T|}{\Phi} \tag{5}$$

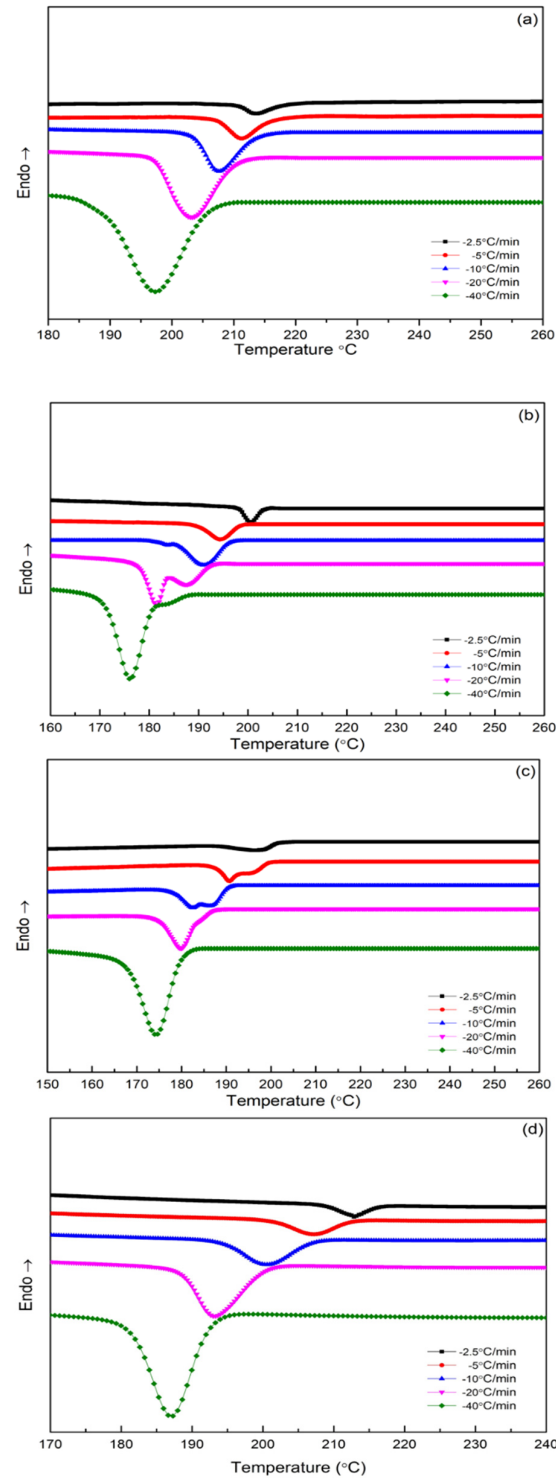


Figure 9. Cont.

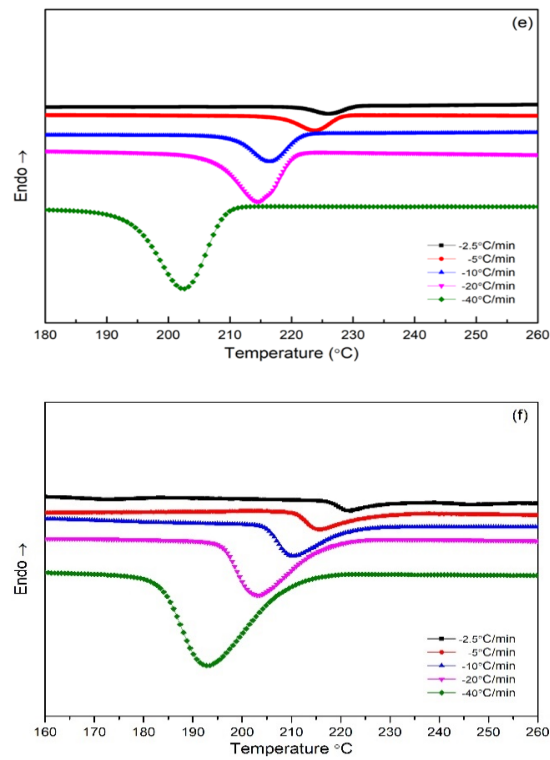


Figure 9. Heat flow versus temperature during nonisothermal crystallization of (a) PA56, (b) CoPA-1, (c) CoPA-2, (d) CoPA-3, (e) CoPA-4 and (f) PA66 at different cooling rates.

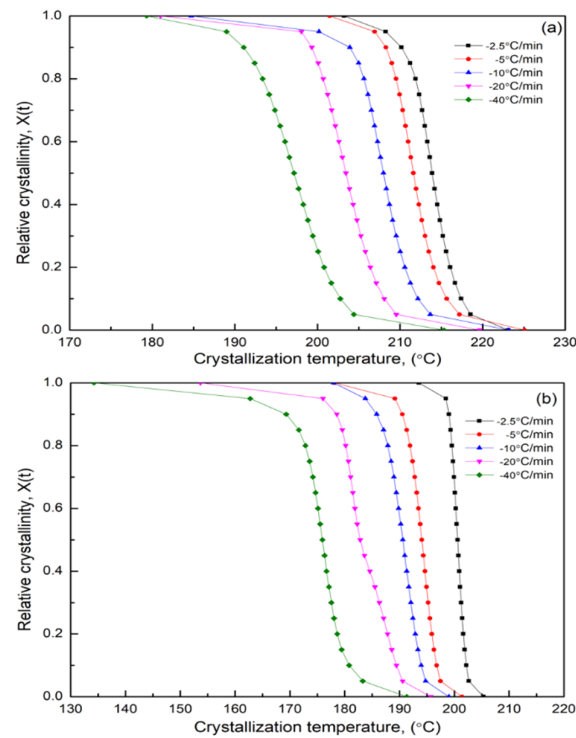


Figure 10. Cont.

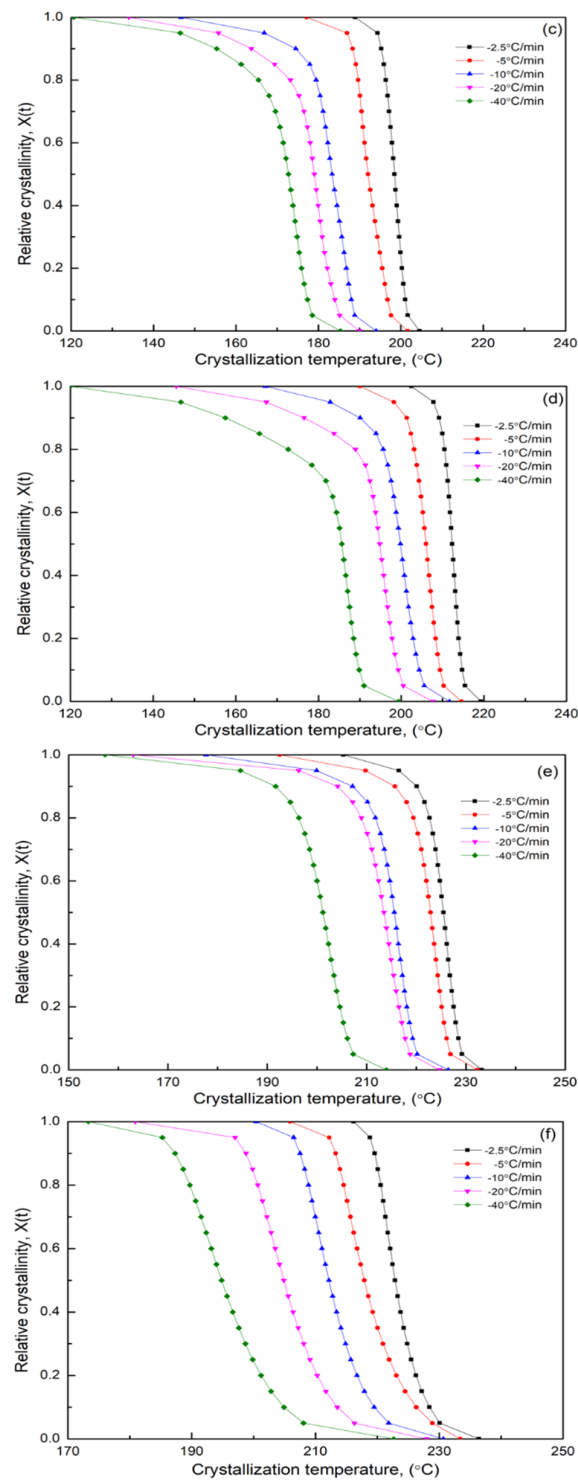


Figure 10. Relative crystallinity $X(t)$ at different crystallization temperatures T in the process of nonisothermal crystallization of (a) PA56, (b) CoPA-2, (c) CoPA-3, (d) CoPA-4, (e) CoPA-5 and (f) PA66.

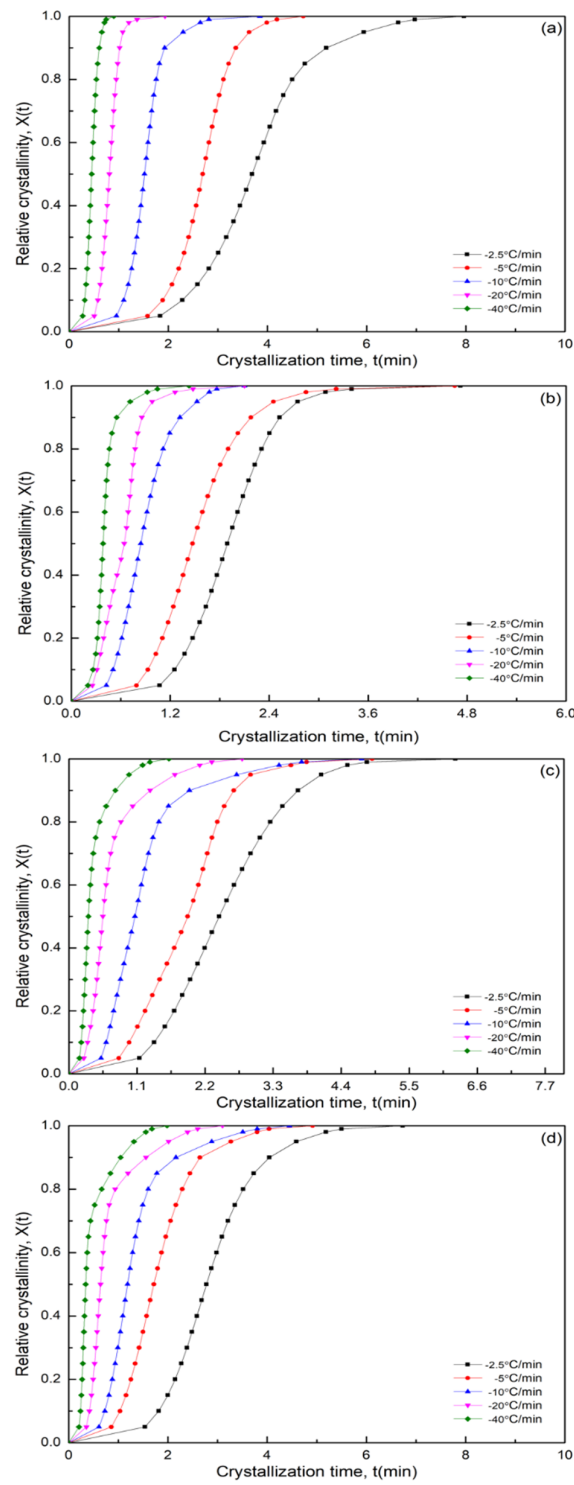


Figure 11. Cont.

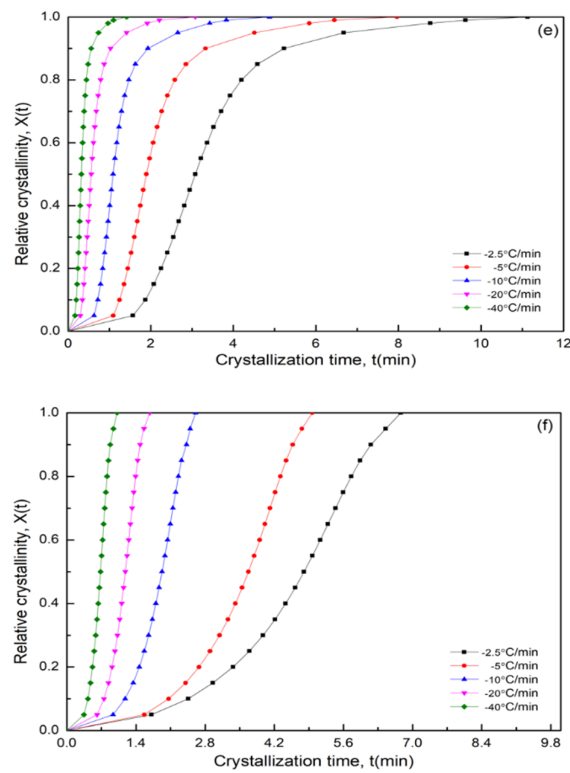


Figure 11. Relative crystallinity $X(t)$ at different crystallization times t in the process of nonisothermal crystallization of (a) PA56, (b) CoPA-2, (c) CoPA-3, (d) CoPA-4, (e) CoPA-5 and (f) PA66.

Table 5. Nonisothermal crystallization parameters of PA56/66 copolyamides at different cooling rates.

Sample	Φ ($^{\circ}\text{Cmin}^{-1}$)	T^* ($^{\circ}\text{C}$)	T_{max} (min)	$X(t_{max})$ (%)	$t_{1/2}$ (min)	$\tau_{1/2}$ (min^{-1})
PA56	2.5	213.63	3.800	54.66	3.691	0.2709
	5	211.25	2.767	55.87	2.694	0.3712
	10	207.67	1.547	54.31	1.519	0.6583
	20	203.34	0.813	51.19	0.811	1.2330
	40	197.32	0.453	48.57	0.454	2.2026
CoPA-1	2.5	200.50	1.933	53.23	1.893	0.5283
	5	194.34	1.413	45.26	1.470	0.6803
	10	191.00	0.800	40.01	0.842	1.1876
	20	181.34	0.713	66.75	0.642	1.5576
	40	176.00	0.383	49.00	0.385	2.5974
CoPA-2	2.5	198.96	2.237	41.64	2.430	0.4415
	5	190.76	2.203	67.39	1.919	0.5211
	10	183.34	1.070	56.27	1.066	0.9381
	20	179.66	0.520	43.26	0.548	1.8248
	40	172.76	0.313	38.46	0.314	3.1847
CoPA-3	2.5	212.35	2.777	45.15	2.778	0.3600
	5	206.59	1.597	42.05	1.716	0.5828
	10	199.00	1.267	48.55	1.186	0.8432
	20	195.66	0.603	41.09	0.902	1.1086
	40	186.68	0.313	39.09	0.342	2.9240
CoPA-4	2.5	226.04	2.847	41.37	3.079	0.3248
	5	223.75	1.717	37.85	1.895	0.5277
	10	216.50	1.005	38.50	1.089	0.9183
	20	214.66	0.503	37.83	0.559	1.7889
	40	202.68	0.280	36.54	0.320	3.1250
PA66	2.5	236.33	1.687	48.75	1.701	0.5879
	5	231.34	1.497	49.25	1.509	0.6627

Table 5. Cont.

Sample	Φ (°Cmin ⁻¹)	T^* (°C)	T_{max} (min)	$X(t_{max})$ (%)	$t_{1/2}$ (min)	$\tau_{1/2}$ (min ⁻¹)
	10	225.33	0.987	49.47	0.988	1.0121
	20	218.34	0.663	47.83	0.676	1.4793
	40	209.32	0.420	52.69	0.410	2.4390

The plots of crystallization t on the x -axis are displayed in Figure 11. All these curves exhibited similar sigmoidal profiles.

The crystallization process was determined to be highly dependent on temperature. The most common approach for describing isothermal crystallization kinetics is the classical Avrami equation [57–59]:

$$X(t) = 1 - \exp(-kt^n) \quad (6)$$

which is often written in a double logarithmic form as follows:

$$\log\{-\ln[1 - X(t)]\} = \log k + n \log t \quad (7)$$

where n is the Avrami exponent, which is dependent on the type of nucleation process; t is the time; and k is the crystallization rate constant involving both nucleation and growth parameters. The crystallization half-time, $t_{1/2}$ is described as the time at which the relative degree of crystallization is equal to 50% and can be calculated from the following equation:

$$t_{1/2} = \left[\frac{\ln 2}{k} \right]^{\frac{1}{n}} \quad (8)$$

The rate of crystallization G is the reciprocal of $t_{1/2}$; $G = \tau_{1/2} = (t_{1/2})^{-1}$. The values of $t_{1/2}$ and $\tau_{1/2}$ are listed in Table 5. The $t_{1/2}$ values decreased as the cooling rate increased for each sample. The $t_{1/2}$ values for the PA56/PA66 co-PAs were lower than that for neat PA56. The parameter t_{max} indicates the time required to achieve the maximum crystallization rate. Because t_{max} corresponds to the point at which $dQ(t)/dt = 0$, $Q(t)$ can be defined as follows:

$$t_{max} = \left(\frac{n-1}{nk} \right)^{\frac{1}{n}} \quad (9)$$

As shown in Figure 9, t_{max} values were derived from the heat flow curves by using Equation (9). The t_{max} value of the PA56 sample was higher than those of neat PA66 and PA56/PA66 co-PAs (Table 5).

3.7.1. Modified Avrami Equation by Jeziorny

Under the assumption of a constant crystallization temperature, Mandelkern [60] described that the primary stage of nonisothermal crystallization using the Avrami equation as follows:

$$1 - X(t) = \exp[-Z_t t^n] \quad (10)$$

$$\log\{-\ln[1 - X(t)]\} = n \log t + \log Z_t \quad (11)$$

where Z_t is a growth rate constant involving nucleation and growth rate parameters and n is the mechanism constant, which depends on the type of nucleation and growth process. To use the equation for analyzing nonisothermal crystallization behavior, Jeziorny [61] considered that the values of Z_t determined by the Avrami equation should be modified as follows:

$$\log Z_c = \frac{\log Z_t}{\Phi} \quad (12)$$

On the basis of Equations (7) and (8), we created plots of $\log\{-\ln[1 - X(t)]\}$ versus $\log t$ (Figure 12). The values of n , Z_t and Z_c were determined from the slope and intercept

of the plots. For the nonisothermal crystallization process (Figure 12), the values of n , Z_t , and Z_c for the PA56/PA66 co-PAs at each cooling rate are listed in Table 6. The curves derived for the PA56/PA66 co-PAs were divided into two sections representing the primary crystallization stage and secondary crystallization stage. The curves indicated the occurrence of a secondary crystallization stage in the nonisothermal crystallization processes of the PA56/PA66 co-PAs. Therefore, the fitting area was selected within the relative crystallinity range of 0–80%. During the initial primary stages of crystallization, the Avrami exponent n_1 varied from approximately 2.68 to 5.26 for CoPA-1, 2.74 to 3.81 for CoPA-2, 3.61 to 4.56 for CoPA-3 and 3.46 to 4.04 for CoPA-4, indicating the occurrence of a three-dimensional growth phenomenon [57]. Compared with the values of n_1 , those of n_2 were 1.21–2.71 for CoPA-1, 1.01–2.73 for CoPA-2, 0.96–2.41 for CoPA-3, and 0.97–1.20 for CoPA-4; these values considerably decreased because of spherulite impingement in the later stages of crystallization [62,63]. The Avrami exponent n_2 was approximately 1 (Table 6), and this was attributed to spherulite impingement and crowding. When the spherulites exhibited one-dimensional growth, the crystallization mode became simpler [64] during the secondary stage. The Z_t values were strongly dependent on the cooling rate and increased with the cooling rate; this is because at higher cooling rates, crystallization occurred at lower temperatures. Compared with the values of Z_t at the same cooling rate, the crystallization rate constant Z_t for the PA56/PA66 copolymers was higher than that derived for the neat PA56 sample, and CoPA-2 exhibited a higher crystallization rate.

Table 6. The values of n , Z_t and Z_c from the Avrami equation at the two stages of nonisothermal crystallization.

Sample	Φ ($^{\circ}\text{Cmin}^{-1}$)	Primary Crystallization Stage			Secondary Crystallization Stage		
		n_1	Z_{t1}	Z_{c1}	n_2	Z_{t2}	Z_{c2}
PA56	2.5	4.110	0.003	0.101	2.304	0.051	0.304
	5	5.576	0.003	0.308	2.981	0.064	0.577
	10	5.787	0.006	0.755	2.084	0.526	0.938
	20	5.455	2.136	1.039	1.262	3.098	1.058
	40	4.755	28.78	1.088	3.454	12.70	1.066
CoPA-1	2.5	4.491	0.039	0.273	2.713	0.178	0.502
	5	3.875	0.151	0.685	2.010	0.466	0.858
	10	3.511	1.235	1.021	2.206	10.09	1.260
	20	2.679	2.584	1.049	1.391	2.800	1.053
	40	5.257	102.0	1.123	1.209	4.413	1.038
CoPA-2	2.5	3.219	0.040	0.275	2.727	0.064	0.333
	5	2.739	0.121	0.656	2.102	0.278	0.774
	10	3.095	0.583	0.948	1.083	1.067	1.000
	20	3.169	4.533	1.079	1.015	1.841	1.031
	40	3.808	55.17	1.107	1.054	3.264	1.030
CoPA-3	2.5	4.350	0.009	0.145	2.409	0.067	0.340
	5	3.611	0.098	0.628	1.728	0.401	0.833
	10	3.774	0.360	0.903	1.183	0.909	0.991
	20	4.241	4.461	1.078	0.992	1.621	1.042
	40	4.564	86.70	1.118	0.958	2.458	1.028
CoPA-4	2.5	3.491	0.013	0.177	1.195	0.304	0.621
	5	3.922	0.053	0.555	1.080	0.600	0.903
	10	4.042	0.412	0.915	1.035	1.120	1.011
	20	3.457	4.866	0.968	0.967	2.134	1.039
	40	3.517	36.15	1.094	1.099	4.159	1.036
PA66	2.5	3.609	0.101	0.399	3.007	0.149	0.467
	5	3.698	0.150	0.684	2.409	0.351	0.881
	10	3.715	0.721	0.968	1.965	1.1153	1.001
	20	4.240	3.597	1.066	1.066	2.321	1.043
	40	4.579	49.64	1.097	1.097	8.447	1.055

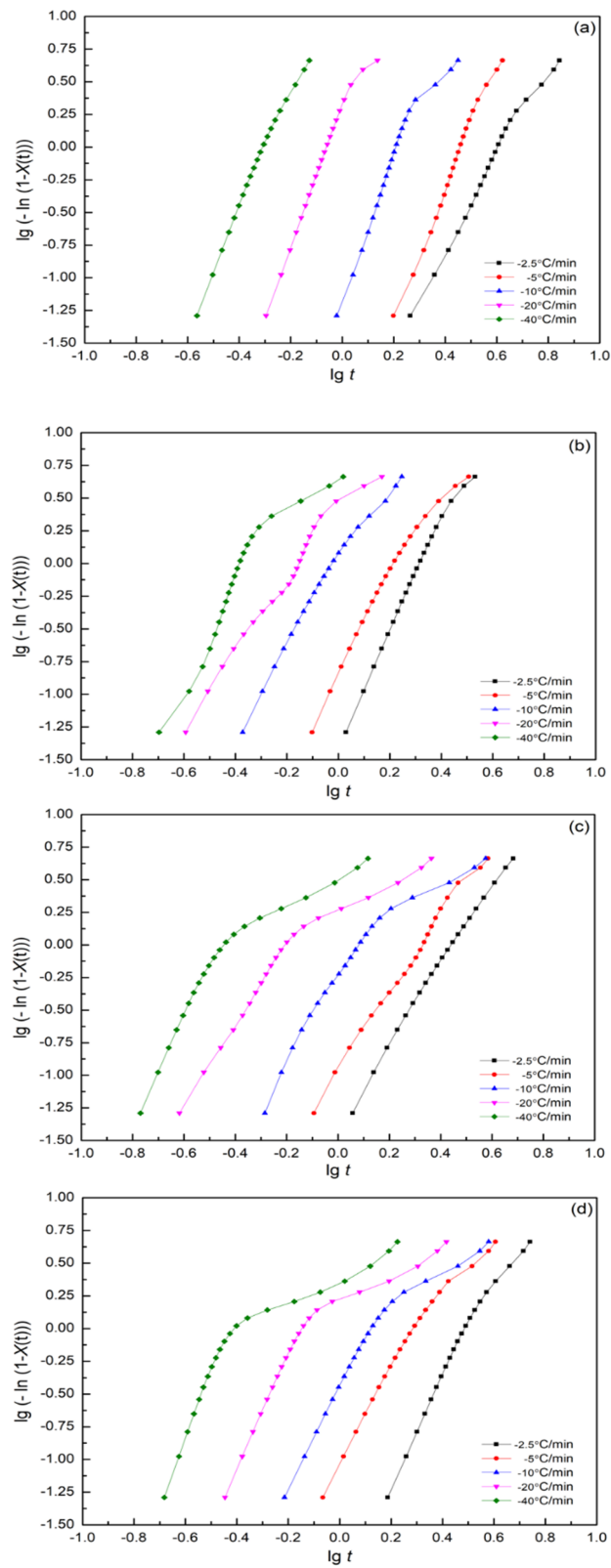


Figure 12. Cont.

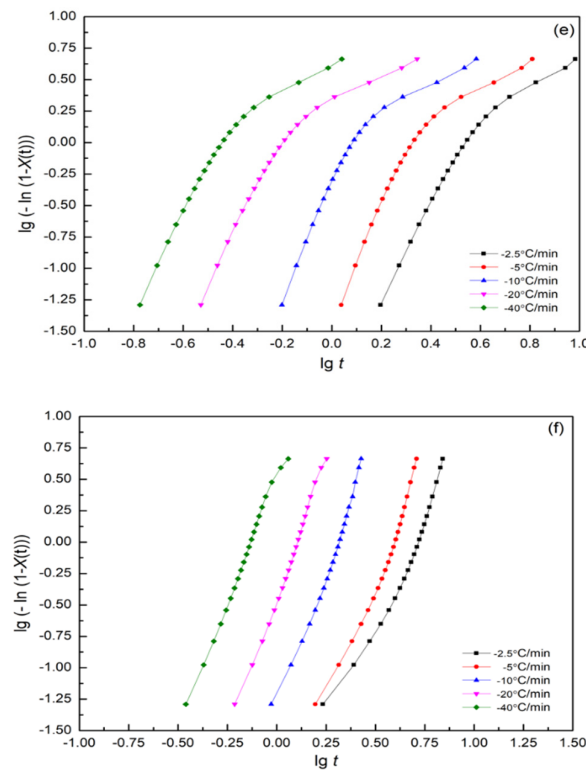


Figure 12. Plots of $\log\{-\ln[1-x(t)]\}$ versus $\log t$ for the nonisothermal crystallization of (a) PA56, (b) CoPA-1, (c) CoPA-2, (d) CoPA-3, (e) CoPA-4 and (f) PA66.

3.7.2. Mo Method

To develop a more appropriate model for depicting nonisothermal crystallization, Mo [65,66] has adopted a convenient approach that entails combining the Avrami equation with the Ozawa equation. The Mo equation can be used to efficiently describe nonisothermal crystallization and successfully characterize the nonisothermal crystallization behaviors of nylon 11 [62], nylon 12 [63], nylon 66 [67], nylon 69 [68], nylon 46 [69], nylon 1212 [70] and biobased nylon composites [71,72]. Accordingly, the following equations can be derived:

$$\log Z_t + n \log t = \log K(T) - m \log \Phi \tag{13}$$

$$\log \Phi = \frac{1}{m} \log \left[\frac{K(T)}{Z_t} \right] - \frac{n}{m} \log t \tag{14}$$

where the parameters $F(T) = [K(T)/Z_t]^{1/m}$ and $a = n/m$; a is the ratio between the Avrami and Ozawa exponents, the parameter $F(T)$ refers to the value of cooling rate chosen set at a unit crystallization time at which the system has a certain degree of crystallinity. The smaller the value of $F(T)$, the higher the crystallization rate becomes. On the basis of these assumptions, the following equation can be derived:

$$\log \Phi = \log F(T) - a \log t \tag{15}$$

According to Equation (15), at a given degree of crystallinity of the PA56/PA66 co-PAs, plotting of $\log \Phi$ versus $\log t$ (Figure 13) yields a linear relationship between $\log \Phi$ and $\log t$. Using a straight line to fit these data points, we obtained straight lines with a slope of $-a$ and intercept of $\log F(T)$. It can be seen from Table 7 that $F(T)$ increases with the increase in the relative degree of crystallinity. The values of a remained almost constant during the crystallization of each sample, indicating that the model of crystallization did not change during crystallization. It can be seen that the $F(T)$ value of PA56/PA66 co-PAs (Table 7) increase with the increase in relative crystallization, and indicates that a higher cooling rate is required to quickly reach a higher relative crystallinity when they crystallize

from melt. Therefore, the Mo model could accurately account for the nonisothermal crystallization kinetics of the PA56/PA66 co-PAs. By contrast, the crystallization model changed depending on the PMD/HMD ratio, signifying that the PMD/HMD ratio affected the model of crystallization of PA56/PA66 co-PAs. At a particular relative crystallinity, the $F(T)$ values derived for the PA56/PA66 co-PAs were lower than that derived for the neat nylon PA56 sample, with the value for CoPA-2 being the lowest. These results were consistent with those obtained using the Jeziorny method.

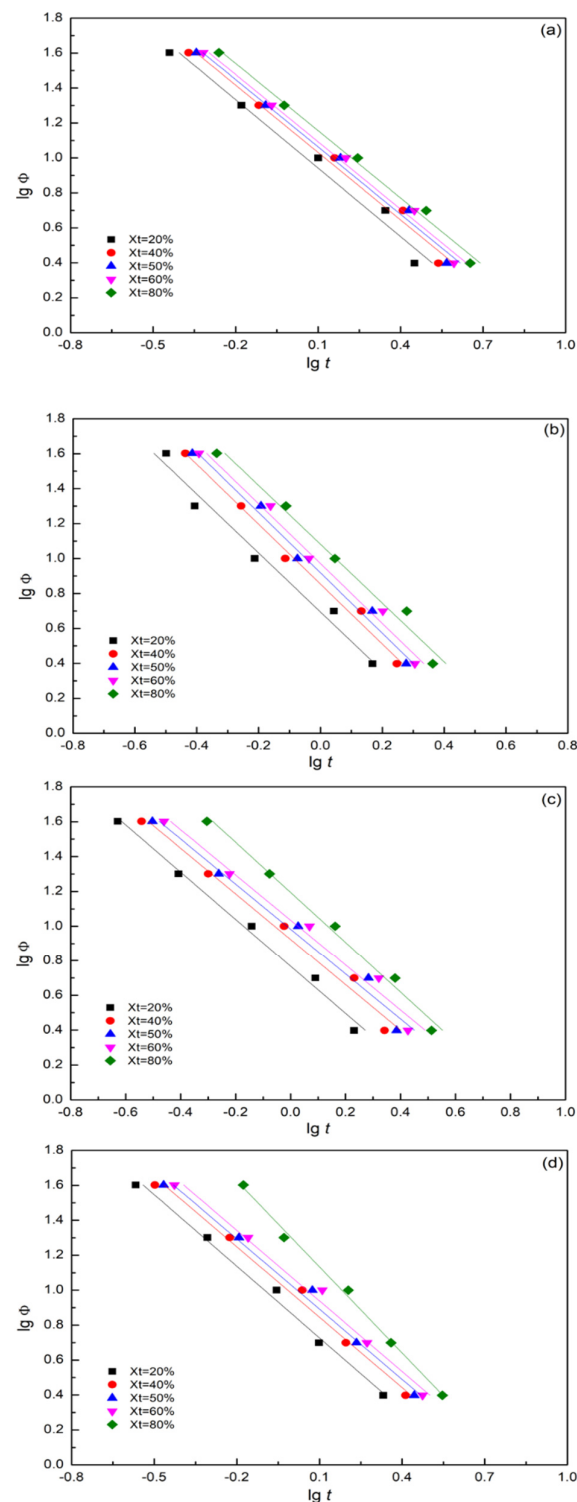


Figure 13. Cont.

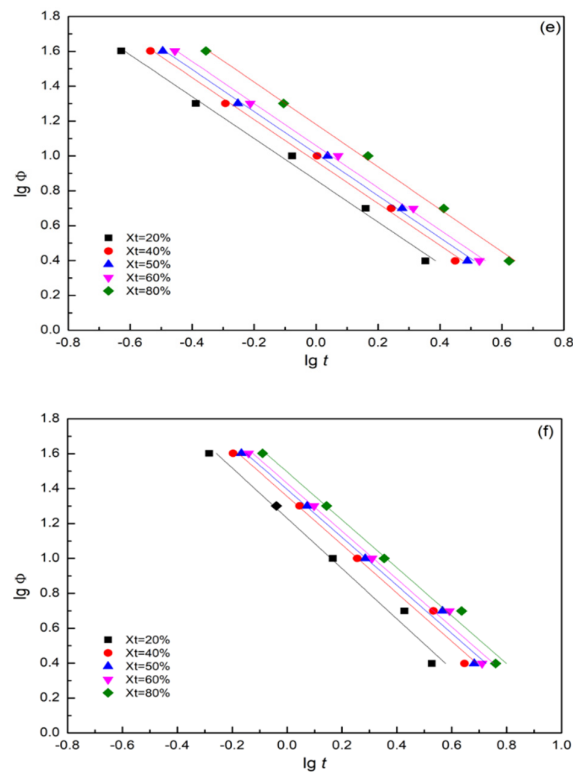


Figure 13. Plots of $\log \Phi$ versus $\log t$ for nonisothermal crystallization of (a) PA56, (b) CoPA-1, (c) CoPA-2, (d) CoPA-3, (e) CoPA-4 and (f) PA66 at different values of relative crystallinity.

Table 7. Nonisothermal crystallization kinetics by the Mo method.

Sample	$Xt(\%)$	a	$F(T)$
PA56	20	1.143	12.62
	40	1.152	14.94
	50	1.161	15.93
	60	1.169	16.90
	80	1.190	19.30
CoPA-1	20	1.588	5.294
	40	1.608	7.575
	50	1.591	8.831
	60	1.558	9.972
	80	1.496	12.75
CoPA-2	20	1.240	6.503
	40	1.159	9.268
	50	1.136	10.40
	60	1.141	11.66
	80	1.313	15.98
CoPA-3	20	1.323	7.509
	40	1.268	9.892
	50	1.255	10.99
	60	1.256	12.20
	80	1.621	19.77
CoPA-4	20	1.121	7.739
	40	1.144	9.647
	50	1.153	10.61
	60	1.160	11.71
	80	1.168	15.33
PA66	20	1.696	6.062
	40	1.631	8.712
	50	1.611	9.906

Table 7. Cont.

Sample	Xt(%)	<i>a</i>	<i>F(T)</i>
	60	1.591	11.12
	80	1.558	14.20

4. Conclusions

First, the PA56/PA66 co-PAs with various comonomer contents were successfully synthesized using in situ polycondensation. The structures of the co-PAs were analyzed through FT-IR spectroscopy and ¹H-NMR. The crystalline structures, morphologies, melting behaviors, crystallization behaviors, and eutectic behaviors of PA56/PA66 were investigated using WAXD, POM and DSC. Both PA56 and PA66 exhibited a eutectic melting point when the PA56 content was 50 mol%, and they demonstrated the most disordered molecular structure, as well as a low melting and crystallization temperatures. In addition, the POM results indicate that the size of spherulites in PA56/PA66 was significantly small and that the number of spherulites was large; therefore, several “induced nuclei sites” were formed because of the reordering of the hydrogen bonds inside the copolymer system. Furthermore, the tensile strength and flexural modulus first decreased and then increased as the PA66 content increased. TGA revealed that the obtained co-PAs possessed excellent thermal stability. This study also investigated the nonisothermal crystallization kinetics of the PA56/PA66 co-PAs through DSC. The equations presented by Jeziorny and Mo were employed to evaluate the nonisothermal crystallization kinetics of the PA56/66 co-PAs. The results obtained using the Jeziorny equation indicated that the nonisothermal crystallization could involve a two-stage process. In the primary stage, the *n*₁ value ranged from 2 to 6, corresponding to a three-dimensional and complex mechanism. In the secondary stage, the *n*₂ value ranged from 1 to 3. The *n*₂ value decreased relative to the *n*₁ value because of spherulite impingement and crowding. The Mo equation was used to successfully describe the two stages of the nonisothermal crystallization process of PA56/PA66. The values of *F(T)* derived for PA56/PA66 strongly depended on the crystallization rate and were lower than those derived for neat PA56 at the same relative crystallinity. The crystallization rates of the PA56/PA66 co-PAs increased relative to that of neat PA56. Therefore, The PA66 may serve as a nucleating agent for crystallization.

Author Contributions: Conceptualization, C.-H.T. and P.-S.T.; methodology, C.-H.T. and P.-S.T.; software, C.-H.T.; validation, C.-H.T. and P.-S.T.; formal analysis, C.-H.T.; investigation, C.-H.T.; resources, C.-H.T.; data curation, C.-H.T.; writing—original draft preparation, C.-H.T. and P.-S.T.; writing—review and editing, C.-H.T. and P.-S.T.; visualization, C.-H.T.; supervision, P.-S.T. All authors have read and agreed to the published version of the manuscript.

Funding: This research received no external funding.

Institutional Review Board Statement: Not applicable.

Informed Consent Statement: Not applicable.

Data Availability Statement: The data presented in this study are available on request from the corresponding author.

Conflicts of Interest: The authors declare no conflict of interest.

References

1. Carothers, W.H. Synthetic Fiber. U.S. Patent 2,130,948A, 20 September 1938.
2. Kohan, M.I. *Nylon Plastics Handbook*; Hanser Publishers: New York, NY, USA, 1995.
3. Liu, B.; Hu, G.; Zhang, J.; Yan, W. Non-isothermal crystallization, yellowing resistance and mechanical properties of heat resistance nylon 10T/66/titania dioxide/glass fibre composites. *RSC Adv.* **2019**, *9*, 7057–7064. [[CrossRef](#)] [[PubMed](#)]
4. Zhang, Y.; Sun, L.; Li, L.; Huang, B.; Wang, T.; Wang, Y. Direct injection molding and mechanical properties of high strength steel/composite hybrids. *Compos. Struct.* **2019**, *210*, 70–81. [[CrossRef](#)]

5. Biricik, G.D.; Celebi, H.; Seyhan, A.T.; Ates, F. Thermal and mechanical properties of flax char/carbon fiber reinforced polyamide 66 hybrid composites. *Polym. Compos.* **2022**, *43*, 503–516. [[CrossRef](#)]
6. Cho, B.G.; Lee, J.E.; Hwang, S.H.; Han, J.H.; Chae, H.G.; Park, Y.B. Enhancement in mechanical properties of polyamide 66-carbon fiber composites containing graphene oxide-carbon nanotube hybrid nanofillers synthesized through in situ interfacial polymerization. *Compos. Part A Appl. Sci. Manuf.* **2020**, *135*, 105938. [[CrossRef](#)]
7. Wang, Z.; Wei, T.; Xue, X.; He, M.; Xue, J.; Song, M.; Wu, S.; Kang, H.; Zhang, L.; Jia, Q. Synthesis of fully bio-based polyamides with tunable properties by employing itaconic acid. *Polymer* **2014**, *55*, 4846–4856. [[CrossRef](#)]
8. Mutua, F.N.; Cheng, C.; Dong, Y.; Zheng, C.; Zhu, B.; He, Y. Synthesis and properties of bio-based poly(pentamethylene oxamide). *Polym. Eng. Sci.* **2017**, *58*, 659–664. [[CrossRef](#)]
9. Lee, J.A.; Ann, J.H.; Kim, I.; Li, S.; Lee, Y. Synthesis, characterization and application of fully bio-based and biodegradable nylon-4,4 and -5,4. *ACS Sustain. Chem. Eng.* **2020**, *8*, 5604–5614. [[CrossRef](#)]
10. Lee, M.O.; Kim, J.H.; Park, J.Y.; Kim, S.Y. Bio-based poly(pentamethylene sebacamide) by solid-state polymerization from bio-based monomers. *Green Chem.* **2021**, *23*, 6469–6476. [[CrossRef](#)]
11. Eltahir, Y.A.; Saeed, H.A.M.; Xia, Y.M.; Wang, Y.M. Preparation of polyamide 5,6 (PA56) fibers and its mechanical properties. *Adv. Mater. Res.* **2014**, *937*, 86–91. [[CrossRef](#)]
12. Kim, H.T.; Baritugo, K.A.; Oh, Y.H.; Hyun, S.M.; Khang, T.U.; Kang, K.H.; Jung, S.H.; Song, B.K.; Park, K.; Kim, I.; et al. Metabolic engineering of *Corynebacterium glutamicum* for the high-level production of cadaverine that can be used for the synthesis of biopolyamide 510. *ACS Sustain. Chem. Eng.* **2018**, *6*, 5296–5305. [[CrossRef](#)]
13. Meng, C.; Liu, X. Synthesis of bio-based semi aromatic high temperature polyamide PA5T/56 and effect of benzene ring on non-isothermal crystallization kinetics. *J. Polym. Res.* **2021**, *28*, 383. [[CrossRef](#)]
14. Gale, E.F.; Epps, H.M. Studies on bacterial amino-acid decarboxylases: 1. l(+)-lysine decarboxylase. *Biochem. J.* **1944**, *38*, 232–242. [[CrossRef](#)]
15. Buschke, N.; Schroeder, H.; Wittmann, C. Metabolic engineering of *Corynebacterium glutamicum* for production of 1,5-diaminopentane from hemicellulose. *Biotechnol. J.* **2011**, *6*, 306–307. [[CrossRef](#)]
16. Kind, S.; Wittmann, C. Bio-based production of the platform chemical 1,5-diaminopentane. *Appl. Microbiol. Biotechnol.* **2011**, *91*, 1287–1296. [[CrossRef](#)]
17. Takahashi, E.; Furui, M.; Seko, H.; Shibatani, T. D-lysine production from L-lysine by successive chemical racemization and microbial asymmetric degradation. *Appl. Microbiol. Biotechnol.* **1997**, *47*, 347–351. [[CrossRef](#)]
18. Xue, C.; Hsu, K.M.; Chiu, C.Y.; Chang, Y.K.; Ng, I.S. Fabrication of bio-based polyamide 56 and antibacterial nanofiber membrane from cadaverine. *Chemosphere* **2021**, *266*, 128967. [[CrossRef](#)]
19. Liu, B.; Zhang, S.; Wang, X.; Yu, J.; Ding, B. Efficient and reusable polyamide-56 nanofiber/nets membrane with bimodal structures for air filtration. *J. Colloid Interface Sci.* **2015**, *457*, 203–211. [[CrossRef](#)]
20. Gadowski, A. Improvement of color value of bio-based polyamide 56 fibers. *e-Polymers* **2018**, *18*, 91–95.
21. Gong, X.; Zhang, S.; Wang, J. Mixed versus networked bio-based PA56/Polyethylene terephthalate composite yarns: A study of two modification methods. *J. Biobased Mater. Bioenergy* **2021**, *15*, 90–96.
22. Stouffer, J.M.; Howard, W.; Starkweather, J.; Hsiao, B.S.; Avakian, P.; Jones, G.A. Copolymer modification of nylon-6,6 with 2-methylpentamethylenediamine. *Polymer* **1996**, *37*, 1217–1228. [[CrossRef](#)]
23. Chen, C.W.; Hsu, T.S.; Huang, K.W.; Rwei, S.P. Effect of 1,2,4,5-benzenetetracarboxylic acid on unsaturated poly(butylene adipate-co-butylene itaconate) copolyesters: Synthesis, non-isothermal crystallization kinetics, thermal and mechanical properties. *Polymers* **2020**, *12*, 1160. [[CrossRef](#)]
24. Lin, C.; Zou, F.; Fernández-Ronco, M.P.; Yan, Y.; Hufenus, R. Melting behavior and non-isothermal crystallization kinetics of copolyimide 6/12. *Polym. Cryst.* **2019**, *2*, 10054.
25. Qu, C.; Tang, Y.; Wang, D.; Fan, X.P.; Li, H.F.; Liu, C.W.; Su, K.; Zhao, D.X.; Jing, J.Q.; Zhang, X. Improved processability of PA66-polyimide copolymers with different polyimide contents. *J. Appl. Polym. Sci.* **2020**, *138*, 49640. [[CrossRef](#)]
26. Xu, Q.; Guan, B.; Guo, W.; Liu, X. Effect of antioxidants on thermo-oxidative stability and aging of bio-based PA56T and fast characterization of anti-oxidation performance. *Polymers* **2022**, *14*, 1280. [[CrossRef](#)]
27. Rwei, S.P.; Ranganathan, P.; Chiang, W.Y.; Lee, Y.H. Synthesis of low melting temperature aliphatic-aromatic copolyamides derived from novel bio-based semi aromatic monomer. *Polymers* **2018**, *10*, 793. [[CrossRef](#)]
28. Feng, W.; Wang, P.; Zou, G.; Ren, Z.; Ji, J. Synthesis and characterization of semiaromatic copolyimide 10T/1014 with high performance and flexibility. *Des. Monomers Polym.* **2018**, *21*, 33–42. [[CrossRef](#)]
29. Yu, A.J.; Evans, R.D. Isomorphous replacement in copolyamide systems: Adipic and terephthalic acids. *J. Polym. Sci.* **1960**, *42*, 249–257. [[CrossRef](#)]
30. Garmans, R.J.; Aalto, S.; Maurer, E.H.J. Copolyamide of nylon-4,6 and nylon-4,T. *J. Polym. Part A Polym. Chem.* **1989**, *27*, 423–430. [[CrossRef](#)]
31. Novitsky, T.F.; Lange, C.A.; Mathias, L.J.; Osborn, S.; Ayotte, R.; Manning, S. Eutectic melting behavior of polyamide 10,T-co-6,T and 12,T-co-6,T copolyterephthalamides. *Polymer* **2010**, *51*, 2417–2425. [[CrossRef](#)]
32. Li, Y.; Liu, H.; Zhang, Y.; Yang, G. Melting behavior and nonisothermal crystallization kinetics of polyamide 6/polyamide 66 molecular composites via in situ polymerization. *J. Appl. Polym. Sci.* **2005**, *98*, 2172–2177. [[CrossRef](#)]

33. Ridgway, J.S. Structure-property relationships of ring-containing nylon 66 copolyamides. *J. Polym. Sci. Part A-1 Polym. Chem.* **1970**, *8*, 3089–3111. [[CrossRef](#)]
34. Vyazovkin, S.; Burnham, A.K.; Criado, J.M.; Pérez-Maqueda, L.A.; Popescu, C.; Sbirrazzuoli, N. ICTAC Kinetics Committee recommendations for performing kinetic computation on thermal analysis data. *Thermochim. Acta* **2011**, *520*, 1–19. [[CrossRef](#)]
35. Vyazovkin, S.; Chrissafis, K.; Lorenzo, M.L.D.; Koga, N.; Pijolat, M.; Roduit, B.; Sbirrazzuoli, N.; Suñol, J.J. ICTAC Kinetics Committee recommendations for collecting experimental thermal analysis data for kinetic computations. *Thermochim. Acta* **2014**, *590*, 1–23. [[CrossRef](#)]
36. Bradbury, E.M.; Brown, L.; Elliott, A.; Parry, D.A.D. The structure of the gamma form of polycapromide (Nylon 6). *Polymer* **1965**, *6*, 465–482. [[CrossRef](#)]
37. Wang, Y.; Kang, H.L.; Guo, Y.F.; Liu, R.G.; Hao, X.M.; Qiao, R.R.; Yan, J.L. The structure and properties of bio-based polyamide 56 fibers prepared by high-speed spinning. *J. Appl. Polym. Sci.* **2020**, *137*, 49344. [[CrossRef](#)]
38. Cooper, S.J.; Coogan, M.; Everall, N.; Priestnall, I. A polarized μ -FTIR study on a model system for nylon 66: Implication for the nylon Brill structure. *Polymer* **2001**, *42*, 10119–10132. [[CrossRef](#)]
39. Cui, X.; Liu, Z.; Yan, D. Synthesis and characterization of novel even-odd nylons based on undecanedioic acid. *Eur. Polym. J.* **2004**, *40*, 1111–1118. [[CrossRef](#)]
40. Pepin, J.; Gaucher, V.; Lefebvre, J.M.; Stroeks, A. Biaxial stretching behavior as a probe of H-bond organization in semi-crystalline polyamides. *Polymer* **2016**, *101*, 217–224. [[CrossRef](#)]
41. Ma, Y.Y.; Zhang, J.; Cao, X.; Wu, P.F.; Ye, G.; Fu, Y.; Zhuang, Y.F.; Zhang, A.; Zheng, K.; Ma, Y.M. High heat resistance and good melt spinnability of a polyamide 66 containing benzene structure. *Mater. Adv.* **2021**, *2*, 6647–6654. [[CrossRef](#)]
42. Ge, H.; Wang, W.; Pan, Y.; Yu, X.; Hu, W.; Hu, Y. An inherently flame-retardant polyamide containing a phosphorus pendent group prepared by interfacial polymerization. *RSC Adv.* **2016**, *6*, 81802–81808. [[CrossRef](#)]
43. Rwei, S.P.; Tseng, Y.C.; Chiu, K.C.; Chang, S.M.; Chen, Y.M. The crystallization kinetics of nylon 6/6T and nylon 66/6T copolymers. *Thermochim. Acta* **2013**, *555*, 37–45. [[CrossRef](#)]
44. Rwei, S.P.; Ranganathan, P.; Lee, Y.H. Isothermal crystallization kinetics study of fully aliphatic PA6 copolyamides: Effect of novel long-chain polyamide salt a comonomer. *Polymers* **2019**, *11*, 472. [[CrossRef](#)]
45. Jia, F.; Mao, J.L.; Ma, Y.; Yao, C. Mechanical and thermal properties of dimer acid based nylon 636/nylon 66 copolymers. *J. Appl. Polym. Sci.* **2014**, *131*, 39845. [[CrossRef](#)]
46. Moran, C.S.; Barthelon, A.; Pearsall, A.; Mittal, V.; Dorgan, J.R. Biorenewable blends of polyamide-4,10 and polyamide-6,10. *J. Appl. Polym. Sci.* **2016**, *133*, 43626. [[CrossRef](#)]
47. Sweet, G.E.; Bell, J.P. Multiple endotherm melting behavior in relation to polymer morphology. *J. Polym. Sci. Part A-2 Polym. Phys.* **1972**, *10*, 1273–1283. [[CrossRef](#)]
48. Harvey, E.D.; Hybart, F.J. Rates of crystallization of copolyamides. II. Random copolymers of nylon 66 and 6. *J. Appl. Polym. Sci.* **1970**, *14*, 2133–2143. [[CrossRef](#)]
49. Bunn, C.W.; Garner, E.V. The crystal structures of two polyamides ('Nylon'). *Proc. R. Soc. Lond. Ser. A Math. Phys. Sci.* **1947**, *189*, 39–68.
50. Yang, T.; Gao, Y.; Wang, X.; Ma, B.; He, Y. Hydrogen bonding and crystalline structure of bio-based PA56. *Polymer* **2021**, *237*, 124356. [[CrossRef](#)]
51. Puiggali, J.; Franco, L.; Alemán, C.; Subirana, J.A. Crystal structure of nylon 5,6. A model with two hydrogen bond directions for derived from odd diamines. *Macromolecules* **1998**, *31*, 8540–8548. [[CrossRef](#)]
52. Morales-Gámez, L.; Soto, D.; Franco, L.; Puiggali, J. Brill transition and melt crystallization of nylon 56: An odd-even polyamide with two hydrogen-bonding directions. *Polymer* **2010**, *51*, 5788–5798. [[CrossRef](#)]
53. Magill, J.H. Spherulitic crystallization. Part I. "Odd-even" polyamides: Nylon 56 and nylon 96. *J. Polym. Sci. Part A* **1965**, *3*, 1195–1219.
54. Tseng, C.H.; Tsai, P.S. The isothermal and nonisothermal crystallization kinetics and morphology of solvent-precipitated nylon 66. *Polymers* **2022**, *14*, 442. [[CrossRef](#)] [[PubMed](#)]
55. Taib, R.M.; Tham, C.Y. Isothermal crystallization kinetics and spherulite morphologies of poly(lactic acid)/ethylene acrylate copolymer blends. *J. Appl. Polym. Sci.* **2017**, *134*, 45487.
56. Song, J.; Ren, M.; Chen, Q.; Sun, X.; Zhang, H.; Song, C.; Zhang, H.; Mo, Z. Isothermal and nonisothermal crystallization kinetics of irradiated nylon 1212. *J. Polym. Sci. Part B Polym. Phys.* **2005**, *43*, 2326–2333. [[CrossRef](#)]
57. Avrami, M. Kinetics of phase change. I General theory. *J. Chem. Phys.* **1939**, *7*, 1103–1112. [[CrossRef](#)]
58. Avrami, M. Kinetics of phase change. II Transformation to relations for random distribution of nuclei. *J. Chem. Phys.* **1940**, *8*, 212–224. [[CrossRef](#)]
59. Avrami, M. Granulation, phase change, and microstructure kinetics of phase change. III. *J. Chem. Phys.* **1941**, *9*, 177–184. [[CrossRef](#)]
60. Wunderlich, B. *Macromolecular Physics*; Academic Press: New York, NY, USA, 1977; Volume 2.
61. Jeziorny, A. Parameters characterizing the kinetics of the non-isothermal crystallization of poly(ethylene terephthalate) determined by d.s.c. *Polymer* **1978**, *19*, 1142–1144. [[CrossRef](#)]
62. Liu, S.; Yu, Y.; Cui, Y.; Zhang, H.; Mo, Z. Isothermal and nonisothermal crystallization kinetics of nylon-11. *J. Appl. Polym. Sci.* **1998**, *70*, 2371–2380. [[CrossRef](#)]

63. McFerran, N.L.A.; Armstrong, C.G.; McNally, T. Nonisothermal and isothermal crystallization kinetics of nylon-12. *J. Appl. Polym. Sci.* **2008**, *110*, 1043–1058. [[CrossRef](#)]
64. Bosq, N.; Aht-Ong, D. Nonisothermal crystallization behavior of poly (butylene succinate)/NaY zeolite nanocomposites. *Macromol. Res.* **2018**, *26*, 13–21. [[CrossRef](#)]
65. Addonizio, M.L.; Martuscelli, E.; Silvestre, C. Study of the non-isothermal crystallization of poly(ethylene oxide)/poly(methyl methacrylate) blends. *Polymer* **1987**, *28*, 183–188. [[CrossRef](#)]
66. Liu, T.; Mo, Z.; Zhang, H. Isothermal and nonisothermal melt crystallization kinetic behavior of Poly(Aryl Ether Biphenyl Ether Ketone Ketone): PEDEKK. *J. Polym. Eng.* **1998**, *18*, 283–299. [[CrossRef](#)]
67. Zhang, Q.; Mo, Z. Melting crystallization behavior of nylon 66. *Chin. J. Polym. Sci.* **2001**, *19*, 237–246.
68. Sun, Z.; Wang, X.; Guo, F.; Jiang, C.; Pan, Q. Isothermal and nonisothermal crystallization kinetics of bio-sourced nylon 69. *Chin. J. Chem. Eng.* **2016**, *24*, 638–645. [[CrossRef](#)]
69. Zhang, Q.; Zhang, Z.; Zhang, H.; Mo, Z. Isothermal and nonisothermal crystallization kinetics of nylon 46. *J. Polym. Sci. Part B Polym. Phys.* **2002**, *40*, 1784–1793. [[CrossRef](#)]
70. Liu, M.; Zhao, Q.; Wang, Y.; Zhang, C.; Mo, Z.; Cao, S. Melting behaviors, isothermal and non-isothermal crystallization kinetics of nylon 1212. *Polymer* **2003**, *44*, 2537–2545. [[CrossRef](#)]
71. Wang, Y.; Kang, H.L.; Wang, R.; Liu, R.G.; Hao, X.M. Crystallization of polyamide 56/polyamide 66 blends: Nonisothermal crystallization kinetics. *J. Appl. Polym. Sci.* **2018**, *135*, 46409. [[CrossRef](#)]
72. Ai, T.; Zou, G.; Feng, W.; Ren, Z.; Li, F.; Wang, P.; Lu, B.; Ji, J. Synthesis and properties of biobased copolyamides based on polyamide 10T and polyamide 56 through one-pot polymerization. *New J. Chem.* **2021**, *45*, 14677–14686. [[CrossRef](#)]